AIAA JOURNAL
Vol. 40, No. 2, February 2002

Mean Flow Features Around the Inline Wheels of Four-Wheel Landing Gear

Barry S. Lazos*
NASA Langley Research Center, Hampton, Virginia 23681

Landing gear are noted to be a significant, sometimes dominant, airframe noise source for commercial aircraft. Aerodynamic noise is a direct result of the fluctuating flow and its interaction with surface components. Knowledge of the mean flow, however, can be used to aid in the determination of noise sources. The complex geometry of multiple-wheel-set landing gear has thus far precluded even this basic information. In this study the mean flowfield is determined in a streamwise plane surrounding the inline wheels of a generic four-wheel landing-gear configuration using digital particle image velocimetry. The velocity and vorticity fields highlight a vortex that persists between the wheels on the ground side of the axle midplane. The formation of this vortex is believed to result from the geometric asymmetry caused by the presence of the center support strut. Evidence is also presented that shows the vortex does not remain stationary, but oscillates between the fore and aft wheels. Its position is hypothesized to depend on the state of an unstable vorticity layer that develops on the ground side of the fore wheel.

I. Introduction

RETRACTABLE landing gear have in the past been considered in a very utilitarian manner as a component performing its function, however important, over a short extent of the aircraft total operation time. Landing gear and their associated flowfields were considered relatively inconsequential to the general performance of the aircraft. Such thinking has resulted in highly nonstreamlined configurations, which include such things as circular tubing in a range of diameters, wires, brake calipers, wheel rims, and hub cavities.

In more recent years the noise characteristics of the airframe have been highlighted, particularly during approach, when landing gear are deployed. Landing-gear noise is characterized as largely broadband, ranging in frequency from about 80 Hz to several kilohertz,[1] with a spectral peak in the lower to midrange frequencies. On most commercial aircraft landing-gear noise is quite a significant contributor to the total airframe noise. In fact, for some modern aircraft, such as the Boeing 777 (Sen, R., private telephone communication, May 1996), the landing gear are considered the dominant airframe noise source.

Many of the higher frequencies in the landing-gear noise spectrum can be easily eradicated by simple streamlining. The lower frequencies, however, are produced by the main components of the configuration, which tend to be quite large[2] and are not so easily streamlined. The wheels are particularly problematic as far a streamlining goes because they must maintain their circular configuration, making a bulky cowling the only streamlining possibility. The question is, how much do the wheels contribute to landing-gear noise?

Landing gear on most commercial aircraft consist of one or more side-by-side pairs of wheels, aligned in the streamwise direction. A literature review by the author suggests that multiple-wheel-set configurations are noisier than single-wheel-set configurations. In two consecutive publications Heller and Dobrzynski[3,4] report their findings on scaled models of four-wheel configurations. In the first, noise measurements led the authors to conclude that one of the dominant noise sources for the four-wheel landing gear is "the interaction of the wake from the forward wheel set with the reward wheel set." In the second, unsteady pressure measurements highlighted significant pressure fluctuations on the rear of the fore wheel and the front of the aft wheel. The authors suggest these are caused, respectively, by flow separation from the fore wheel and wake impingement on the aft.

Another point of consideration is the relevance scale-model studies have in understanding full-scale noise production mechanisms because the frequency and amplitude characteristics of model noise do not scale well with those of actual landing gear. Two reasons have been suggested for this scaling disparity. The first is a lack of geometric detail in scale-model experiments.[5,6] Typically, scale models neglect landing-gear details mentioned in the first paragraph of this section. The second is a Reynolds-number dependence of landing-gear noise.[2,7] This is suspected because flow separation and wake features are Reynolds-number dependent and changes in these are likely to affect noise level and frequency.

In an attempt to address these issues, Dobrzynski and Buchholz[6] recently conducted an experiment in the German-Dutch Wind Tunnel utilizing an actual four-wheel landing gear from an Airbus A320 aircraft. Data acquired were analyzed using an "acoustic holographic" technique to determine source levels in a plane about a quarter of a wheel diameter from the axles on the ground side of the axle plane. The results presented suggest significant noise production along the downstream end of the fore wheels in the frequency range between 850 and 950 Hz. The authors state that "tirewake/tire interaction" is not as significant a noise contributor as was previously suspected. They also point out that the source areas identified "cannot easily be correlated with any particular gear structural component." Such an observation may suggest that developed flow structure plays an important role in noise production for this configuration.

Although the scale-model concerns just presented are indeed valid when considering unsteady flow phenomena, such concerns might not be as pressing when considering mean flow development around a configuration. If the Reynolds number is reasonably close to flight conditions, mean flow structure will be similar for scaled and actual configurations. Likewise, depending on the region in which the flow measurements are made, the elimination of configuration details will have a minor effect on the mean flow characteristics. In the present study the mean flow characteristics around a generic configuration of a four-wheel landing gear are considered. The model wheels and struts were scaled to those on a Boeing 757. Configuration details were eliminated to concentrate on the flow characteristics around the wheels. Tests were conducted at a Reynolds number based on wheel diameter of 600,000. Digital particle image velocimetry (DPIV) data were acquired in a plane bisecting the inline wheels in which mean velocity and vorticity fields were calculated. Some static pressure data were also acquired for clarification of flow details. Although this paper is meant to assist in determining regions of the flowfield

Received 21 December 2000; revision received 1 June 2001; accepted for publication 22 June 2001.

*Research Scientist, 1 E. Reid Street.

that might be responsible for significant noise production, noise sources can only be inferred because the fluctuating features responsible for noise production were not measured. This work should be considered as a first step in understanding the flowfield around a four-wheel landing gear, providing information important for computational fluid dynamics validation.

II. Experiments

A. Facility, Model, and Experimental Equipment

Experiments were conducted in the Basic Aerodynamics Research Tunnel (BART)[8] at the NASA Langley Research Center. This facility is an open circuit wind tunnel with a test section area of 71 × 102 cm and a length of 305 cm. The interior of the test section is visually accessible from all sides except the floor. An orthogonal motion traversing rig surrounds the test section and has a location readout accuracy of 10 μ in the x and y directions and 1 μ in the z direction.

The model used in the present study was a generic configuration of a four-wheel landing gear with wheels and struts scaled to 31% of those on a Boeing 757. It was simplified by eliminating detailed components such as tubing, wheel covers, braking mechanisms, bolt heads, etc. Figure 1 is a dimensioned schematic of the model. Two of the model wheels were produced from SL 5180 resin using stereolithography. The other two were molded fiberglass. The cylindrical sections of the support structure and axles were either steel or aluminum. Materials chosen for the model were a result of test and instrumentation requirements.

Figure 2 shows the model installed upside down in the tunnel test section. The origin of the coordinate system used in the current study is shown located on the outboard face of the fore wheel at its center. The plane bisecting the inline wheels, in which DPIV data were acquired, is highlighted. One of the model's wheels was marked with fiduciary points to allow accurate mapping of oil-flow visualization images. Another wheel was outfitted with 50 pressure taps along its periphery and made rotatable using a servomotor installed in the axle. This allowed data to be acquired 360 deg around the wheel. During data acquisition, all wheels were locked in a stationary position. Only partial details of the static pressure data and none of oil-flow visualization data are included in this report.

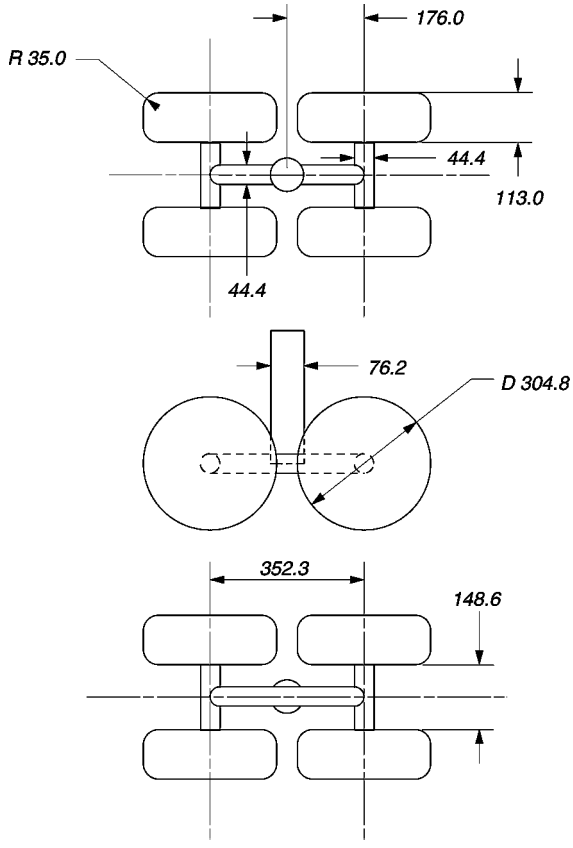

Fig. 1 Dimensioned schematic of 31% scale model of Boeing 757 landing bogie (dimensions in millimeters).

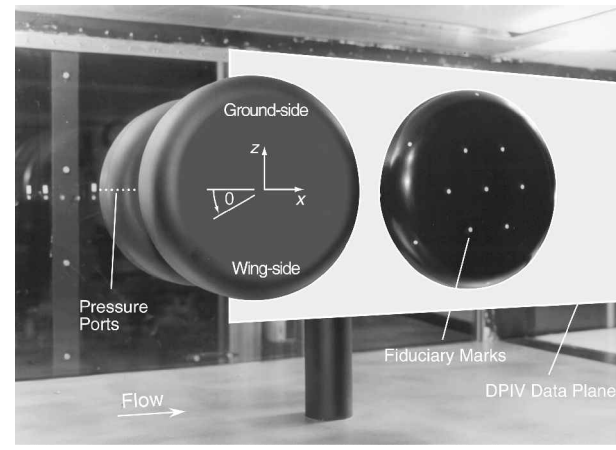

Fig. 2 Model installed in BART facility.

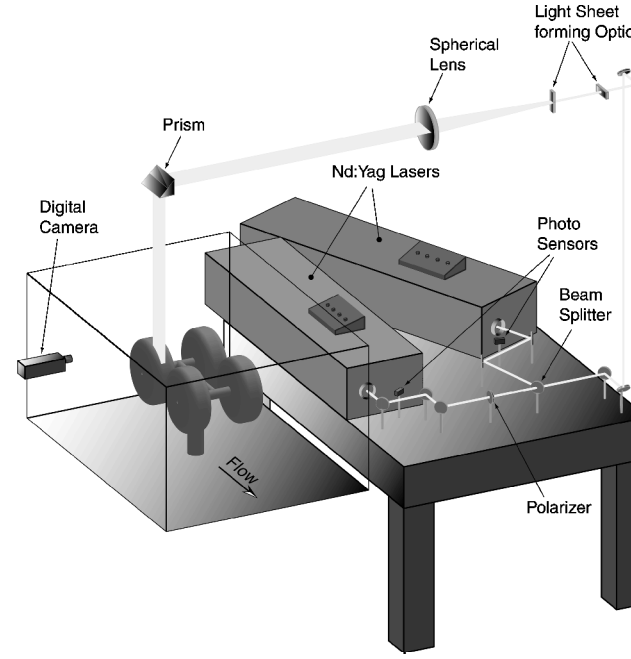

Fig. 3 DPIV equipment setup.

DPIV data images were acquired using a Kodak ES 1.0 digital camera with a pixel resolution of 1018 by 1008. The camera was attached to the traverse mechanism surrounding the facility so that it could be accurately positioned. Two Nd:Yag lasers illuminated the particle field with a nominal 500 mJ of energy per pulse at a 532-nm wavelength. The light-sheet thickness ranged between 1 and 2 mm with adjustments toward the high end made to reduce error caused by out-of-plane motion. Light-sheet thickness was adjusted toward the low end when out-of-plane motion was not a factor to isolate the plane of interest. Firing of the lasers and image acquisition were accomplished through electronic circuitry that coupled the two events together. The delay time Δt between acquisition of the two images in a pair ranged from 2 to 9 μs. Adjustments were made toward the low end to reduce error caused by out-of-plane motion and toward the high end to reduce error caused by small particle displacement. Figure 3 shows the setup for the DPIV system and the placement of the laser light sheet for acquisition of data above the model. Data acquisition on the underside of the model was accomplished by adjusting the light-sheet optics to pass it through a Starfire™ glass window installed in the floor under the wheels.

B. Experimental Data Acquisition and Reduction

The DPIV data plane extended in the streamwise direction from $x = -50$ to 658 mm and in the cross-stream direction from $z = -194$

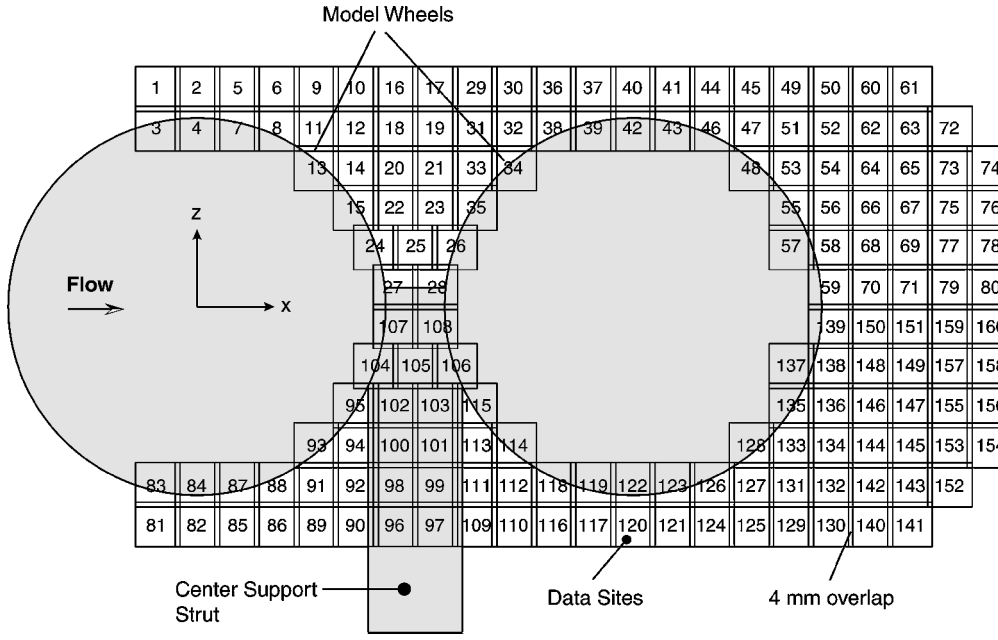

Fig. 4 DPIV data sites bisecting inline wheels of model.

to 194 mm. It consisted of 160 side-by-side image planes measuring 36×36 mm, each overlapping its neighbors by 4 mm. The size of the image planes was made small to provide the spatial resolution necessary for a more detailed future analysis. Figure 4 shows the position of each image plane relative to the coordinate axes located at the center of the fore wheel. At least 100 image pairs were acquired at each data location in groups of 50 at a rate of 5 Hz.

Seeding of the flow was accomplished using four TSI model 9306 six-jet atomizers. The seed material was a common drugstore mineral oil, which, when atomized, produces a median particle size of about 0.7 μ. Because the BART facility is an open circuit tunnel, the entire room enclosing it was filled with particles. This ensured the flow was sufficiently seeded at all data locations, providing an even distribution of particles throughout the tunnel test section.

Interrogation of particle image pairs was performed to determine the velocity vectors associated with the displacement of particles from image one to image two. Critical parameters used in DPIV interrogation are image magnification and the time delay Δt between acquisition of the first and second image in a pair. Image magnification was determined by adjusting the camera lens so that it precisely imaged the width of a square measuring 36×36 mm. With the exact width of the charge-coupled device (CCD) array known, the ratio of the image width to the CCD array width yielded a magnification of four. Accurate measurement of Δt was accomplished using photo sensors to detect the firing of each laser and an electronic counter to determine time between firings to the nanosecond.

The interrogation technique correlated image pairs to provide the three most likely vectors at a given interrogation spot. Each interrogation spot measured 64×64 pixels and overlapped its neighbors by 16 pixels. The three most significant correlation peaks were identified, with each peak located to subpixel accuracy within the interrogation spot using a Gaussian fit. The location of each peak then prescribed the magnitude and direction of the three vectors most likely to originate from the center of the spot. The reduction software colored each vector black, red, or green, in order of significance. Analysis of this sort over the entire image area yielded a 60×60 vector array with a spatial resolution of about 1 mm. During testing, a preliminary analysis was performed on a sample of six vector images from each group of 50, with a temporal spacing of 2 s between each image. If more than 2% of the 3600 most significant vectors were erroneous, laser light intensity, light-sheet thickness, and/or delay time between laser firings were adjusted to reduce the error. After all data sets were acquired, the vector images were postprocessed using a routine called Cleanvec.[9] This routine used statistical information about the surrounding vectors to determine which of the three vectors resulting from the cross correlation was the most appropriate. Each image was then manually checked for significant erroneous vector selection.

III. Results and Discussion

A. Mean Velocity Field in DPIV Data Plane

The mean velocity field in a plane bisecting the inline wheels was determined by averaging together 50 velocity vector images in each of the 160 DPIV data locations. In locations 22 and 23 between the wheels (Fig. 4), neither of the two groups of 50 consecutively acquired images produced an average that matched neighboring average images. This suggested that mean flow conditions were changing between the wheels within the 10-s data acquisition time. A visual analysis of each of the images from these locations revealed variation between two distinct flow patterns. To produce a complete picture of a mean velocity field around the wheels, visual pattern recognition was used to group 50 similar vector images together.

Figure 5 displays a mean velocity field around the wheels using line integral convolution (for more information on this visualization technique see Ref. 10). In the figure streamline features are readily apparent, and velocity magnitude is represented with color. Both separation and attachment locations highlighted in the figure were determined using streamline tracing. On the back of the fore wheel, flow attachment occurs over a range as great as 40 deg from about -150 to -190 deg. Some specific streamlines between the wheels are highlighted in white.

Only two asymmetries are readily apparent around the outside of the wheels: the magnitude of the flow velocity on the wing and ground sides of the aft wheel and the azimuthal locations of flow attachment on the front of the aft wheel. To quantify the latter asymmetry, a closer analysis of the DPIV data was performed. It revealed that flow attaches on the wing side of the aft wheel at 30 deg and on the ground side at -35 deg. This 5-deg offset is believed to allow the formation of the vortex observed between the wheels. Flow stagnation at a lesser angle on the wing side allows fluid from that side to penetrate further into the gap region between the wheels. This shifts the separation location on the front side of the aft wheel toward the ground side and allows the separated fluid to roll up into a vortex behind the fore wheel. This midwheel vortex has the potential to produce significant ground-directed noise because it likely contains turbulent eddies developed in the wake of the fore wheel that scrub against the wheel surface as the vortex rotates near it.

The asymmetric flow conditions observed around the aft wheel are expected to result from differences in the upstream flow conditions on the wing and ground sides of the fore wheel. Figure 6 is a plot of the streamwise velocity profiles on the wing and ground sides of the fore wheel at ± 90 deg, extracted from the DPIV data.

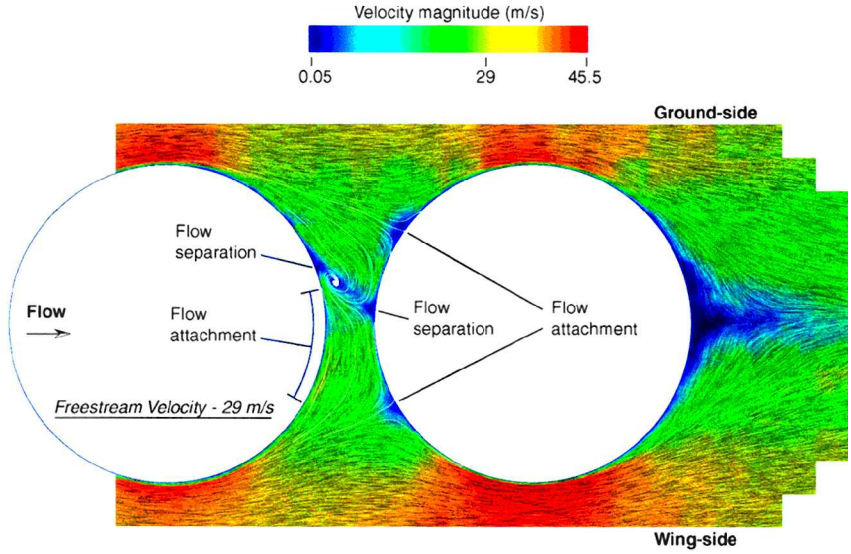

Fig. 5 Velocity magnitude and direction in DPIV plane bisecting inline wheels; streamlines between wheels highlighted in white.

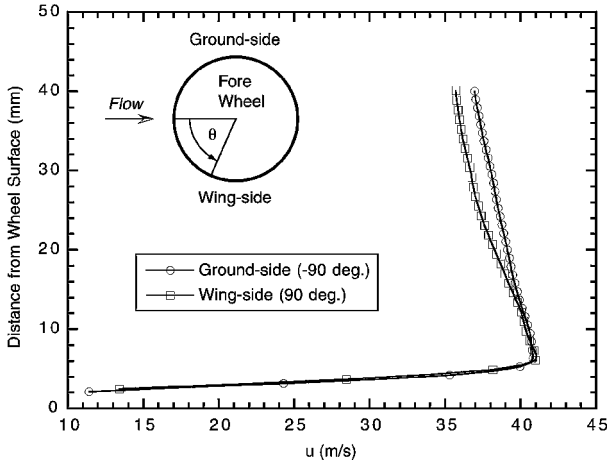

Fig. 6 Streamwise velocity profiles at ± 90 deg on fore wheel.

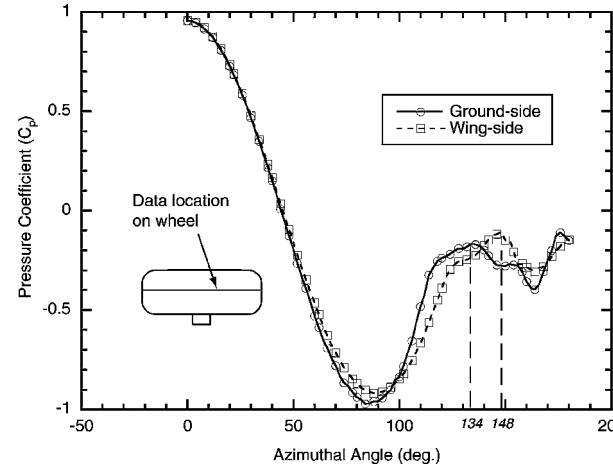

Fig. 7 Mean azimuthal pressure on fore wheel.

The plot shows a velocity defect on the wing side of the wheel as opposed to the ground side. This defect is expected to result from flow obstruction created by the center support strut which is the only geometric asymmetry on the model. To further evaluate flow conditions on the fore wheel, mean pressure data were acquired at a single port around the circumference in 2-deg increments. At each measurement station 30,000 data samples were acquired over a 90-s period using an electronically scanned pressure acquisition system. Positioning accuracy of the wheel was determined to be approximately ±0.3 deg. The data acquired are plotted in Fig. 7 with the data location identified. It reveals that the pressure drops to a lower value on the ground side of the wheel, corresponding to the higher velocity observed on that side in Fig. 6. Also apparent is the more dramatic rise in pressure on the ground side with a peak reached at −134 deg, 14 deg ahead of that on the wing side. To quantify the degree of pressure change around the wheel, values of azimuthal pressure gradient were calculated on both sides using first-order finite differencing. Figure 8 is a plot of these results, and readily apparent are the differences from ground to wing side in the magnitude and location of the adverse pressure gradient peak. The peak on the ground side of the wheel is 50% greater in magnitude and occurs 10 deg ahead of the peak on the wing side. Given the preceding differences in velocity, pressure, and pressure gradient characteristics around the fore wheel, one would suspect that separation on the wing side of the wheel occurs at a greater azimuthal angle than that on the ground side—this being ultimately a result of the geometric asymmetry of the center support strut. Such a delay in separation is hypothesized to result in the asymmetric flow features observed around the aft wheel.

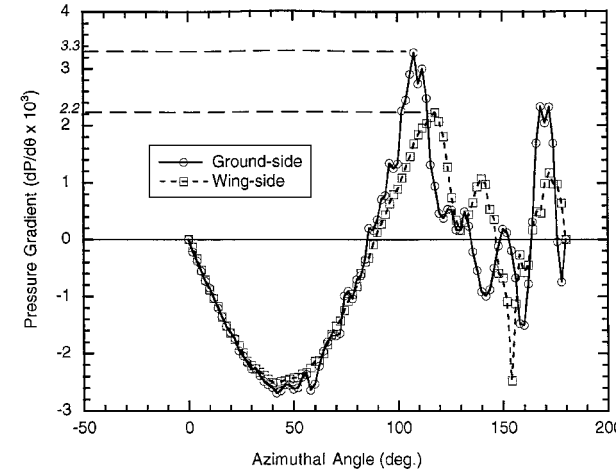

Fig. 8 Azimuthal pressure gradient around fore wheel.

B. Mean Vorticity Field in DPIV Data Plane

The mean vorticity field was calculated in the midplane of the wheels using the definition of circulation and Stokes theorem. A close-up of the region between the wheels is shown in Fig. 9 with color-coded contours representing vorticity level. Away from the wheel surfaces the inviscid nature of the flow results in a near zero mean vorticity. However, the vorticity layers on the wheel surfaces are prominently portrayed as well as the vortex roll up behind

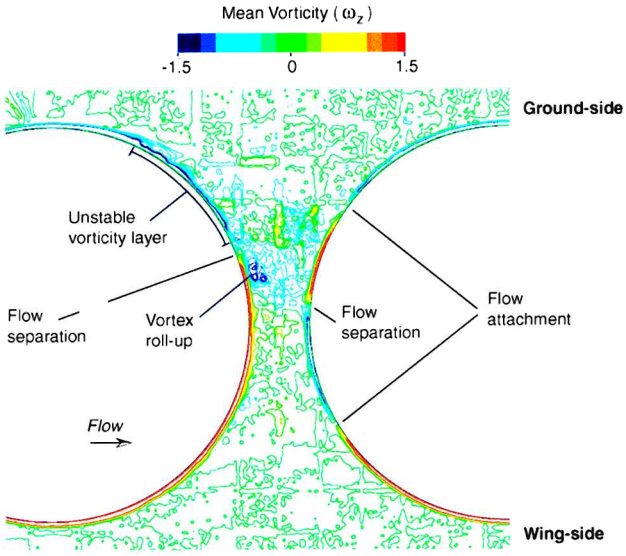

Fig. 9 Mean vorticity field in midplane of wheels.

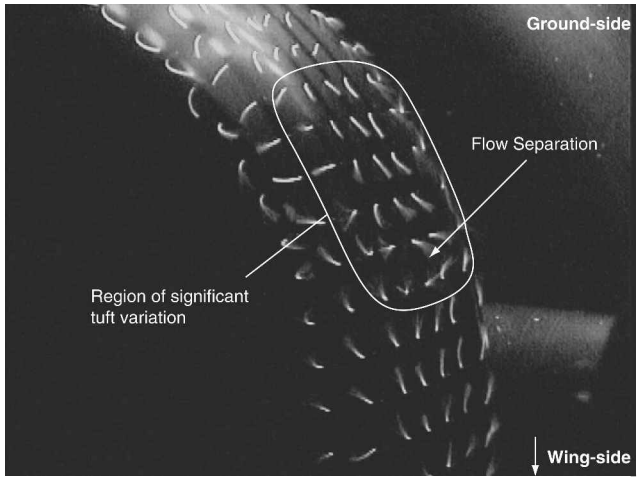

Fig. 10 Tuft markers highlighting flow attachment on backside of fore wheel.

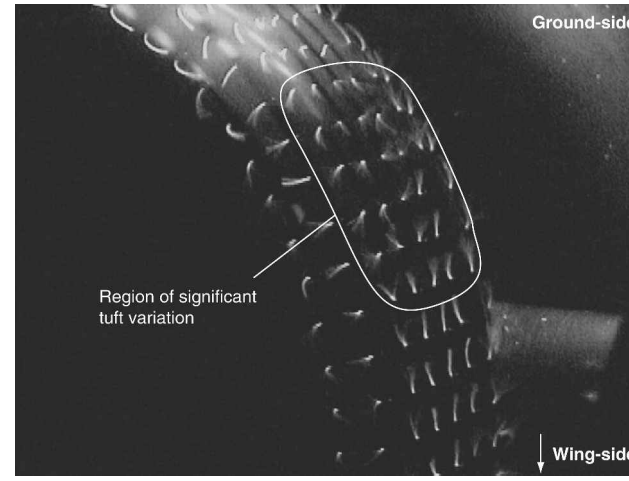

Fig. 11 Tuft markers highlighting flow separation on backside of fore wheel.

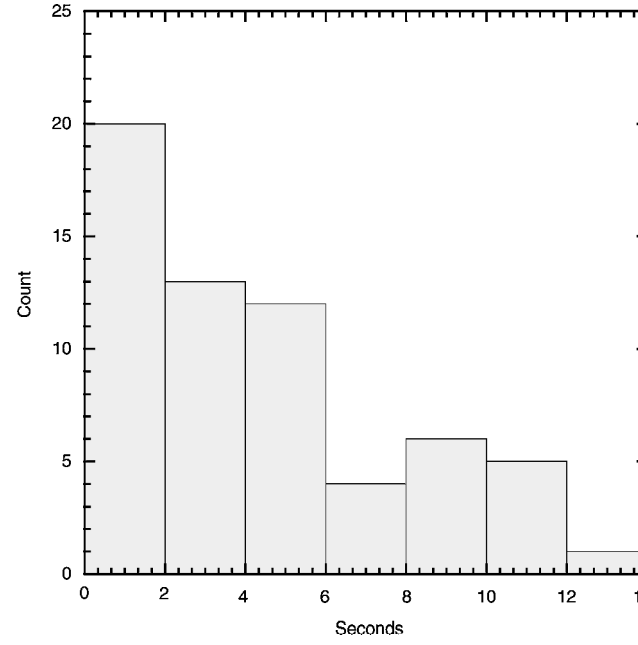

Fig. 12 Histogram of number and duration of observed occurrences of a state of massive flow separation on the backside of the fore wheel.

the fore wheel. Separation and attachment locations on the front of the aft wheel are well-defined at the junction of positive and negative vorticity. Positive vorticity extends around the back side of the fore wheel to about 200 deg from the leading edge. This suggests that, in the mean, the boundary layer originating on the wing side of the fore wheel remains attached, or very nearly attached, over a large extent of the wheels downstream surface and supports the hypothesis of the discussion in the preceding section. On the ground side of the fore wheel, the negative vorticity layer becomes wavy and discontinuous beginning at about −115 deg from the wheel leading edge. This suggests that the vorticity layer in this region is unstable. Such a shear-layer instability would likely result in changing separation characteristics on this side of the wheel with flow remaining attached to the wheel surface at times and separating at others.

To visually establish the separation characteristics on the backside of the fore wheel, fluorescent monofilament minitufts were used. Each tuft was cut to a length of 10 mm and attached to the back of the wheel on a grid with 13 × 13 mm cells. The tuft material had a diameter of 33 μ and was made highly visible with ultraviolet lighting. Video recordings of the tuft activity identified two mean flow states; one appearing to persist a bit longer, on average, than the other. In the first state tuft features suggested flow remained attached to the ground side of the fore wheel to about −160 deg from the wheel leading edge. Here it encountered attached flow from the wing side of the wheel and separated. Figure 10 is an image extracted from the video of tuft orientation when the flow is in this state. The separation location identified in the figure is also highlighted in Fig. 9. In the second state tuft activity suggested massive flow separation along the location marked "unstable vorticity layer" in Fig. 9. In other locations tuft activity remained relatively unaltered. An image from the video of tuft orientation in this second state is shown in Fig. 11.

To quantify the degree to which each state persisted, a 10-min segment of tuft video was digitized and analyzed visually, frame by frame. The results show that over the time period studied, the attached state persisted 57% of the time. A histogram of the number of occurrences of the separated state and their duration is shown in Fig. 12. This figure demonstrates that changes between states was often rapid, with 74% of occurrences lasting 6 s or less. A statistical analysis of the data shows that out of the 61 occurrences of the separated state the mean duration was 4.32 s with a standard deviation of 3.37 s.

C. Off-Surface Flow Feature Difference Between Mean States

With the preceding evidence that separation characteristics on the backside of the fore wheel are continuously changing between two different states, consideration must be given to what effect this will have on other nearby flow features. Of specific interest is the effect this can have on the position and persistence of the vortex observed between the wheels in Figs. 5 and 9. To investigate this, DPIV data sets from locations between the wheels were again analyzed. Recall

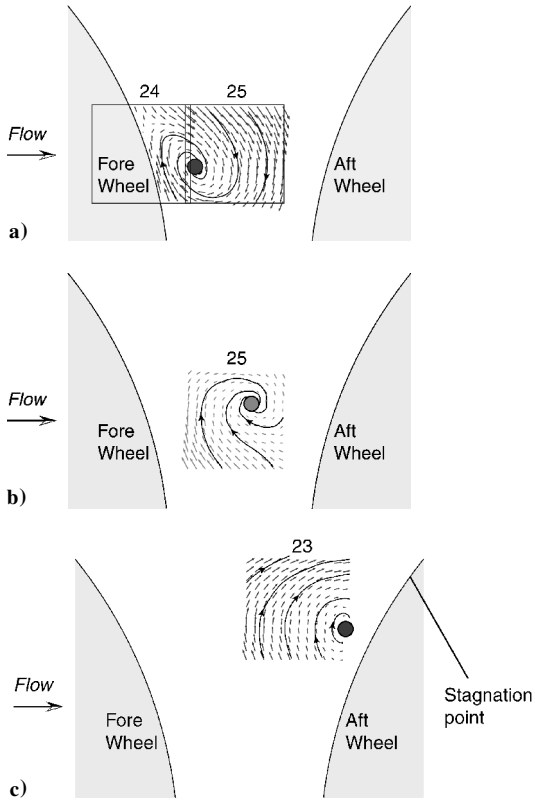

Fig. 13 Position change of vortex between wheels determined from DPIV data.

from Sec. III.A that at certain locations between the wheel the 50 vector images for an averaged data set were accumulated by hand picking images that looked similar in order to match the averaged image to its neighbors. For the current analysis data sets consisted of 50 images acquired consecutively over a 10-s period and were acquired randomly in time. In other words, pattern recognition methods were not used to collect the 50 images that constituted these sets.

The average image of each set reveals an apparent shift in the position of the midwheel vortex. Figure 13 shows three segments of averaged velocity vectors calculated from data sets at locations 23, 24, and 25 (refer to Fig. 4 for a broader view of these locations). The figure suggests the vortex shifts location between the wheels. Such a shift can result in the generation of noise as the vortex collides first with one wheel and then the other. It is hypothesized that in Fig. 13a the shear layer is attached to the surface on the ground side of the fore wheel. Recall that tuft visualization in Sec. III.B identified this as the most persistent mean state. Here the vortex is detected directly behind the fore wheel as was observed in Figs. 5 and 9. As the shear layer begins to separate from the wheel surface, the vortex progresses downstream (Fig. 13b). When the flow on the ground side of the fore wheel is completely separated, the vortex resides directly in front of the aft wheel (Fig. 13c). Although not enough direct evidence is currently available to prove this correlation between separation state on the fore wheel and the midwheel vortex position, the theory is certainly plausible with circumstantial evidence to support it.

IV. Conclusions

The current study examined mean flow features around a four-wheel landing gear. The model used was a generic configuration of a four-wheel landing gear with wheels and struts scaled to 31% of those on a Boeing 757. Tests were conducted at a Reynolds number based on wheel diameter of 600,000. Digital Particle Image Velocity data were acquired and used to determine the mean velocity and vorticity fields in the vertical midplane surrounding the inline wheels.

The results highlight a vortex that persists in the gap between the inline wheels. The vortex is expected to result from a 5-deg azimuthal asymmetry in flow attachment location on the front side of the aft wheel. This asymmetry allows fluid on the wing side of the wheels to penetrate further into the gap region, forcing the development of the vortex on the ground side of a plane passing through the axle centerlines. Evidence suggests the asymmetric flow conditions around the aft wheel result from the geometric asymmetry associated with the center support strut.

Qualitative evaluation of separation characteristics on the backside of the fore wheel using tuft visualization identified two mean flow states, one more prominent than the other. Evaluation of DPIV velocity vector images between the wheels highlighted changes in the position of the midwheel vortex. It is hypothesized that changes in mean flow state between the wheels and changes in the position of the midwheel vortex are directly related. A sequence is postulated to correlate the two events.

The midwheel vortex is a possible source of noise in two ways. In a stationary position resting against a wheel, the vortex will scrub turbulent eddies against the wheel surface. Translation of the vortex between the wheels will also generate noise as it distorts upon collision with one wheel and then the other. Although in this particular study the wheel-to-wheel translation of the vortex was at a relatively low frequency, it can be expected that this frequency will increase with increasing Reynolds number. Noise created by the rotation and translation of the vortex between the wheels will be directed groundward because the vortex is observed to persist on the ground side of the axle midplane.

Acknowledgments

The author would like to thank J. B. Anders and C. Yao at the NASA Langley Research Center as well as D. Rockwell at Lehigh University for their assistance in analyzing and interpreting the data.

References

[1]Delfs, J., and Heller, H. H., "Aeroacoustic Research in Europe—1996 Highlights," *Aerospace Science and Technology*, Vol. 2, No. 2, 1998, pp. 145–154.

[2]Heller, H. H., and Dobrzynski, W. M., "A Comprehensive Review of Airframe Noise Research," *Proceedings of the 11th Congress of the International Council of the Aeronautical Sciences (ICAS)*, Vol. 1, edited by J. Singer and R. Staufenbiel, International Council of the Aeronautical Sciences, Lisbon, 1978, pp. 42–60.

[3]Heller, H. H., and Dobrzynski, W. M., "Sound Radiation from Aircraft Wheel-Well/Landing Gear Configurations," *Journal of Aircraft*, Vol. 14, No. 8, 1977, pp. 768–774.

[4]Heller, H. H., and Dobrzynski, W. M., "Unsteady Surface Pressure Characteristics on Aircraft Components and Farfield Radiated Airframe Noise," AIAA Paper 77-1295, Oct. 1977.

[5]Dobrzynski, W. M., and Buchholz, H., "Full-Scale Noise Testing on Airbus Landing Gears in the German Dutch Wind Tunnel," AIAA Paper 97-1597, 1997.

[6]Heller, H. H., and Dobrzynski, W. M., "Airframe Noise: Recent Results from Experimental Studies on Landing Gears and High-Lift Devices," Aeroacoustics Workshop—Project SWING, Inst. of Acoustics and Speech Communication, Dresden Univ. of Technology, Dresden, Germany, Oct. 1999.

[7]Yamamoto, K. J., Donelson, M. J., Shumei, C. H., and Joshi, M. C., "Airframe Noise Prediction Evaluation," NASA CR-4695, Oct. 1995.

[8]Sellers, W. L., and Kjelgaard, S. O., "The Basic Aerodynamics Research Tunnel-A Facility Dedicated to Code Validation," AIAA Paper 88-1997, May 1988.

[9]Meinhart, C. D., Barnhart, D. H., and Adrian, R. J., "Interrogation and Validation of Three-Dimensional Vector Fields," *Developments in Laser Techniques and Applications to Fluid Mechanics*, edited by R. J. Adrian, D. F. G. Darão, F. Durst, M. V. Heitor, M. Maeda, and J. H. Whitelaw, Springer-Verlag, Berlin, 1994, pp. 379–391.

[10]Cabral, B., and Leedom, L., "Imaging Vector Fields Using Line Integral Convolution," *Computer Graphics Proceedings'93, ACM SIGGRAPH*, 1993, pp. 263–270.

P. J. Morris
Associate Editor

Color reproductions courtesy of NASA Langley Research Center.